
SPHENIC: TOPOLOGY-INFORMED MULTI-VIEW CLUSTERING FOR SPATIAL TRANSCRIPTOMICS

A PREPRINT

 **Chenkai Guo**

Guangzhou Institutes of Biomedicine and Health
Chinese Academy of Sciences
Guangzhou, Guangdong 510530
guochenkai23@mailsucas.ac.cn

 **Yikai Zhu**

College of Medicine and Biological Information Engineering
Northeastern University
Shenyang, Liaoning 110016
yikai.zhu@outlook.com

 **Jing Yangum**

Department of Computer System and Technology
Universiti Malaya
Lembah Pantai, Kuala Lumpur 50603

 **Renxiang Guan**

School of Computer
National University of Defense Technology
Changsha, Hunan 410073
renxiangguan@nudt.edu.cn

 **Por Lip Yee**

Department of Computer System and Technology
Universiti Malaya
Lembah Pantai, Kuala Lumpur 50603
porli@pum.edu.my

 **Guangdun Peng***

Guangzhou Institutes of Biomedicine and Health
Chinese Academy of Sciences
Guangzhou, Guangdong 510530
peng_guangdun@gibh.ac.cn

 **Dayu Hu***

College of Medicine and Biological Information Engineering
Northeastern University
Shenyang, Liaoning 110016
hudy@bmie.neu.edu.cn

August 15, 2025

ABSTRACT

By incorporating spatial location information, spatial-transcriptomics clustering yields more comprehensive insights into cell subpopulation identification. Despite recent progress, existing methods have at least two limitations: (i) topological learning typically considers only representations of individual cells or their interaction graphs; however, spatial transcriptomic profiles are often noisy, making these approaches vulnerable to low-quality topological signals, and (ii) insufficient modeling of spatial neighborhood information leads to low-quality spatial embeddings. To address these limitations, we propose SPHENIC, a novel Spatial Persistent Homology Enhanced Neighborhood Integrative Clustering method. Specifically, SPHENIC incorporates invariant topological features into the clustering network to achieve stable representation learning. Additionally, to construct high-quality spatial embeddings that reflect the true cellular distribution, we design the Spatial Constraint and Distribution Optimization Module (SCDOM). This module increases the similarity between a cell's embedding and those of its spatial neighbors, decreases similarity with non-neighboring cells, and thereby produces clustering-friendly spatial embeddings. Extensive experiments on 14 benchmark spatial transcriptomic slices demonstrate that SPHENIC achieves superior performance on the spatial

*Corresponding authors

clustering task, outperforming existing state-of-the-art methods by 3.31%–6.54% over the best alternative.

Keywords Spatial-transcriptomics clustering · Multi-view clustering · Persistent homology · Graph learning

1 Introduction

Spatial transcriptomics has transformed the study of biological systems by providing spatially resolved gene-expression profiles in intact tissues Rao et al. (2021); Moses and Pachter (2022); Tian et al. (2023); Williams et al. (2022); Jain and Eadon (2024). A critical step in this approach is the accurate spatial clustering required to delineate spatially coherent cellular domains in which cells exhibit both molecular similarity and physical proximity. Accurate identification of these domains may have far-reaching implications, including guiding therapeutic target discovery and advancing our understanding of complex biological systems and cellular behaviors Gulati et al. (2025); Wang et al. (2024).

Current spatial-transcriptomics clustering methods are typically classified into three categories: (i) traditional community-detection approaches (e.g., Seurat and Scanpy), which often prioritize gene expression over spatial organization Wolf et al. (2018); Satija et al. (2015); (ii) deep-learning methods, including stMMR and GraphST, which explicitly model spatial-transcriptional relationships via graph structures to identify biologically relevant spatial domains Zhang et al. (2024); Long et al. (2023); and (iii) supervised methods, such as PASSAGE, that incorporate phenotypic guidance Guo et al. (2025). These latter two classes have attracted considerable attention and are widely regarded as significant improvements over methods that rely solely on gene expression matrix Li et al. (2025).

Despite recent progress, existing spatial clustering approaches have the following limitations: (i) Most methods rely on graph-based representations to capture topological patterns in cellular data (Fig. 1); however, when noise is present, the extracted topological features are often of low quality and unreliable. Some researchers apply persistent homology to learn topological invariants, but this approach can overlook complex multidimensional structures in the data; consequently, learning topology-invariant representations from spatial transcriptomics profiles remains challenging. (ii) Furthermore, most methods construct spatial relationships using simple adjacency graphs, which leads to inadequate modeling of spatial context and produces low-quality embeddings that distort neighborhood relationships in the latent space.

To bridge these gaps, we propose SPHENIC, a spatial clustering method tailored for spatial transcriptomics data. Concretely, SPHENIC extends persistent homology to effectively learn topology-invariant features. Subsequently, it constructs separate views for different modalities and fuses them via a multi-view Graph Convolutional Network (GCN) to learn comprehensive consensus representations. In addition, we develop a Spatial Constraint and Distribution Optimization Module (SCDOM) that further optimizes cell distributions and embedding quality by increasing the similarity between a cell’s embedding and those of its spatial neighbors while decreasing similarity to non-neighboring cells. Extensive experiments demonstrate the superiority of SPHENIC; our main contributions are summarized as follows:

- We pioneer the integration of extended persistent homology into existing spatial clustering frameworks. To the best of our knowledge, this study constitutes the first attempt to incorporate topology-invariant features to enhance spatial clustering.
- We propose a novel SCDOM component that explicitly preserves neighborhood relationships and improves the quality of cell representations. In addition, a zero-inflated negative binomial (ZINB) model is employed to regularize cell expression distributions, thereby mitigating distorted clustering results.
- Extensive experiments have been conducted across three distinct spatial transcriptomics datasets, encompassing a total of 14 tissue slices, demonstrating the consistent superiority of SPHENIC over existing state-of-the-art methods.

2 Related Work

2.1 Clustering in Spatial Transcriptomics

Clustering strategies for spatial transcriptomics data can be broadly classified into three paradigms Liu et al. (2024); Zahedi et al. (2024); Hu et al. (2024); Yuan et al. (2024). (i) Traditional community-detection methods, implemented in tools such as Seurat and SCANPY, employ the Louvain or Leiden algorithm to cluster cells on the basis of gene expression similarity Wolf et al. (2018); Satija et al. (2015); Blondel et al. (2008); Traag et al. (2019). Although computationally efficient, these methods typically treat spatial information as secondary and may therefore overlook

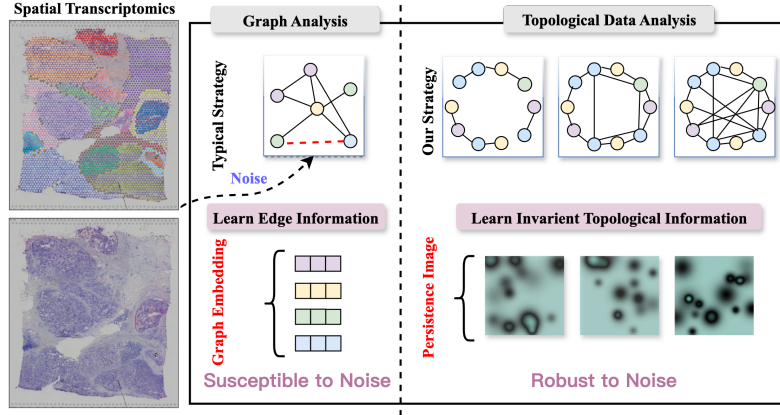


Figure 1: Comparison of graph learning and invariant topological feature learning.

critical aspects of tissue organization. (ii) Deep-learning-based techniques have recently emerged to more effectively integrate spatial context with gene expression. For example, SpaGCN employs GCN to model spatial neighbourhoods, whereas stLearn jointly incorporates expression profiles, spatial coordinates, and histological image features Hu et al. (2021); Pham et al. (2020); Kipf (2016). Spatial-MGCN further advances this paradigm by introducing multi-view graph learning Wang et al. (2023). (iii) Supervised methods leverage phenotypic guidance to delineate biologically meaningful spatial domains and molecular signatures. PASSAGE exemplifies this strategy by learning phenotype-associated signatures through a two-step contrastive graph-learning framework, thereby identifying domains that correspond to known anatomical or pathological phenotypes Guo et al. (2025). However, none of the existing approaches integrates invariant topological information into the spatial clustering process.

2.2 Topological Data Analysis

Topological data analysis leverages algebraic topology to examine complex graph-structured data Pham et al. (2025); Wasserman (2018); Su et al. (2025). Recent progress can be summarized along three key directions: (i) novel network architectures, such as TopoGCL Chen et al. (2024), augment graph neural networks by injecting persistent homology features into the message-passing schema, thereby enabling more robust modeling of higher-order interactions in molecular and social graphs; (ii) regularization techniques, exemplified by TopoReg Chen et al. (2019), introduce filtration-based losses that preserve critical connectivity patterns within latent representations, which significantly improve graph-classification performance; and (iii) generative methods, including TopoDiff Zhang et al. (2025), employ topological signatures to steer the synthesis of graphs possessing desired structural properties, a capability that is particularly valuable for drug-discovery applications. Collectively, these advances demonstrate topology’s transformative potential for graph representation learning by capturing multi-scale relationships, enabling a wide range of biomedical applications Hernández-Lemus et al. (2024); Skaf and Laubenbacher (2022).

3 Methods

In this section, we detail the proposed SPHENIC framework. As illustrated in Fig. 2, the framework consists of three core components: (i) topological representation learning, where we employ extended persistent homology (EPH) to extract topological features from spatial transcriptomics data; (ii) a multi-view GCN fusion network, which integrates expression profiles, spatial context, and topological information through convolutional and attention-based operations; and (iii) a spatial constraint and distribution optimization module (SCDOM) that preserves spatial coherence during training.

3.1 Topology-informed Representation Learning

Spatial transcriptomics data inherently possess topological structure, yet capturing this structure remains challenging. Existing methods learn representations of individual cells or their interaction graphs; however, transcriptomic profiles are often noisy, making these methods susceptible to low-quality topological signals. To address this limitation, we focus on invariant topological features of the cell graph.

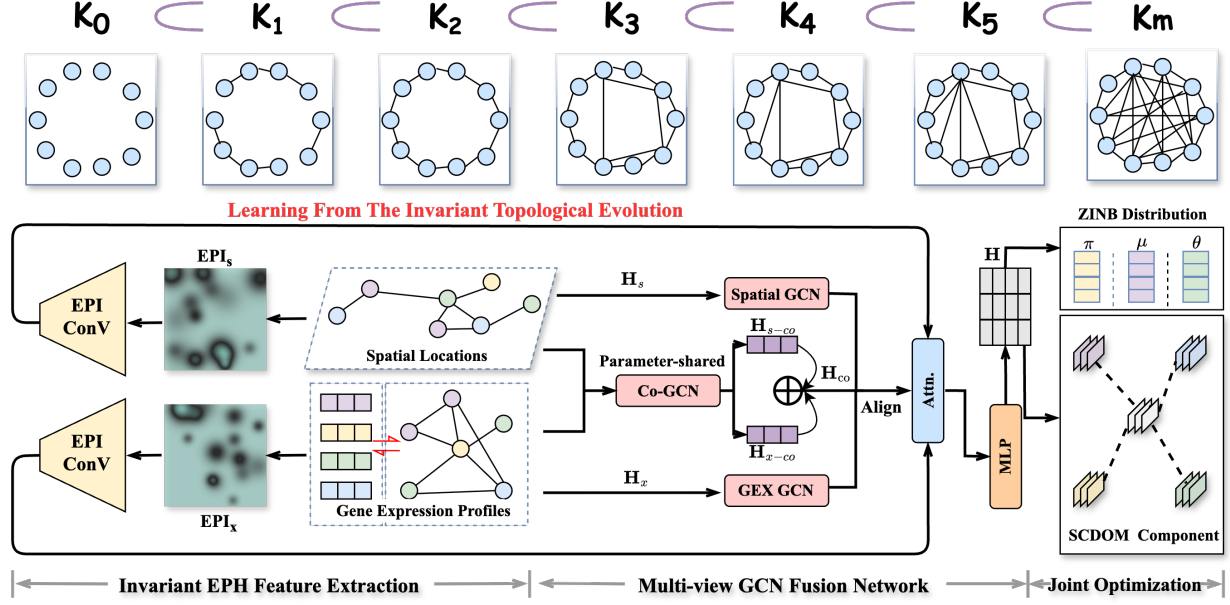


Figure 2: The overall framework of our proposed SPHENIC. Invariant topological information is incorporated into the multi-view graph fusion network to enhance the representation of different cells by EPH feature extraction. Then, the ZINB decoder and SCDOM are designed to ensure the spatial distribution and consistency of spatial clustering results.

Specifically, we employed the EPH method to simultaneously extract topological features from spatial and gene-expression data via a filtration process. Mathematically, we first constructed two weighted graphs:

$$\mathcal{G}_s = (\mathcal{V}, \mathcal{E}_s, \omega_s); \mathcal{G}_x = (\mathcal{V}, \mathcal{E}_x, \omega_x), \quad (1)$$

where the vertex set \mathcal{V} represents individual spatial spots, and edge weights are specified by two functions: $\omega_s: \mathcal{E}_s \rightarrow \mathbb{R}$, encoding Euclidean distances between spatial locations, and $\omega_x: \mathcal{E}_x \rightarrow \mathbb{R}$, encoding dissimilarities between gene-expression profiles. After constructing the graphs, we built filtrations by monotonically increasing the thresholds ϵ_s and ϵ_x while tracking the resulting topological invariants:

$$\begin{aligned} \mathcal{G}_s^{\epsilon_s^{(1)}} \subseteq \mathcal{G}_s^{\epsilon_s^{(2)}} \subseteq \dots \subseteq \mathcal{G}_s^{\epsilon_s^{(n)}} = \mathcal{G}_s; \\ \mathcal{G}_x^{\epsilon_x^{(1)}} \subseteq \mathcal{G}_x^{\epsilon_x^{(2)}} \subseteq \dots \subseteq \mathcal{G}_x^{\epsilon_x^{(n)}} = \mathcal{G}_x. \end{aligned} \quad (2)$$

For each of the two graphs in these filtrations, we constructed the corresponding Vietoris–Rips complex, thereby obtaining a sequence of complexes that records the evolution of topological features, including connected components, cycles, and voids, across both spatial and gene-expression scales.

$$\begin{aligned} \text{VR}_{\epsilon_s^1}(\mathcal{G}_s) \subseteq \text{VR}_{\epsilon_s^2}(\mathcal{G}_s) \subseteq \dots \subseteq \text{VR}_{\epsilon_s^n}(\mathcal{G}_s); \\ \text{VR}_{\epsilon_x^1, r}(\mathcal{G}_x) \subseteq \text{VR}_{\epsilon_x^2, r}(\mathcal{G}_x) \subseteq \dots \subseteq \text{VR}_{\epsilon_x^n, r}(\mathcal{G}_x), \end{aligned} \quad (3)$$

where ϵ_s^i and ϵ_x^i ($i = 1, 2, \dots$) represent the edge-weight thresholds employed to construct the spatial and expression subgraphs, respectively. With these parameters, the Vietoris–Rips filtrations induced by the weight functions ω_s and ω_x capture the evolution of topological features in the lower-star (ascending) and upper-star (descending) directions, yielding the spatial graph filtrations $\mathcal{G}_{(s)}^{\leq \epsilon_i} = (\mathcal{V}, \mathcal{E}_s, \omega_s^{-1}(-\infty, \epsilon_i])$ and $\mathcal{G}_{(s)}^{\leq \epsilon_i} = (\mathcal{V}, \mathcal{E}_s, \omega_s^{-1}[\epsilon_i, \infty))$.

For gene expression (GEX) profiles, we further apply a spatially constrained EPH feature-extraction procedure, parameterized by (i) an edge-weight function ω_x based on expression similarity and (ii) a spatial radius constraint r that explicitly excludes edges exceeding a specified physical distance. This spatial filtration helps preserve biologically meaningful spatial organization of the topological features encoded in the EPD while maintaining relevant expression-based connectivity patterns, thereby yielding GEX filtrations $\mathcal{G}_{(x)}^{\leq \epsilon_i} = (\mathcal{V}, \mathcal{E}_x, \omega_x^{-1}(-\infty, \epsilon_i] \cap \omega_s^{-1}(-\infty, r])$ and $\mathcal{G}_{(x)}^{\leq \epsilon_i} = (\mathcal{V}, \mathcal{E}_x, \omega_x^{-1}[\epsilon_i, \infty) \cap \omega_s^{-1}(-\infty, r])$.

These filtrations encode invariant multiscale topological structure in data. By recording the birth–death pairs (b_s, d_s) and (b_x, d_x) at which each topological feature is born and dies in the above filtrations, we obtain the extended persistence diagram (EPD) for spatial locations and GEX profiles, represented as $\text{EPD}_s = \{(b_s, d_s) \in \mathbb{R}^2\}$ and $\text{EPD}_x = \{(b_x, d_x) \in \mathbb{R}^2\}$, respectively.

The resulting EPD are multisets in \mathbb{R}^2 and therefore are not directly amenable to numerical computation. Thus, we embed each EPD into a functional representation in a Hilbert space, yielding an extended persistence image (EPI). This mapping generates a fixed-dimensional vector representation that is compatible with standard deep-learning architectures while preserving the essential topological information encoded in the EPD. Specifically, each birth-death pair in the EPD is mapped to a weighted Gaussian kernel, yielding a persistence surface ρ_{EPD} , which is the sum of Gaussian functions centered at each birth-death point. Then the persistence surface is discretized by integrating ρ_{EPD} over a predefined grid. Each pixel value $\text{EPI}(p)$ is given by the integral of ρ_{EPD} over the corresponding pixel p , formally expressed as follows:

$$\text{EPI}(p) = \iint_p \sum_{\mu \in \text{EPD}} \frac{\mathcal{F}(\mu)}{2\pi\sigma_x\sigma_y} \times \exp\left[-\frac{(x-b_\mu)^2}{2\sigma_x^2} - \frac{(y-d_\mu)^2}{2\sigma_y^2}\right] dx dy, \quad (4)$$

where $\mathcal{F}(\mu) = |\mu_x - \mu_y|^p$ is the weight function to quantify the persistence time of each birth-death pair. $\mu = (b_i, d_i)$, with $i = 1, 2, \dots$, denotes the individual birth–death pairs in the EPD, and σ_x and σ_y denote the standard deviations of the EPI along the x and y axes, respectively. This procedure ultimately yields EPI for both spatial and GEX profiles.

3.2 Topology-informed Multi-view GCN Fusion

To effectively learn from both spatial and GEX data, while capturing cross-modality biological interdependencies, we construct separate views for each data modality. The resulting views are fused using a multi-view GCN network, which systematically integrates spatial organization, GEX profiles, and EPI information.

3.2.1 View-specific Learning

To incorporate both spatial information and GEX patterns into the proposed model, we apply graph convolutions in parallel to the expression-similarity adjacency matrix \mathbf{A}_x and the spatial adjacency matrix \mathbf{A}_s ; we formalize the operation as follows:

$$\begin{aligned} \mathbf{H}_x^{(l+1)} &= \text{ReLU}\left(\tilde{\mathbf{D}}_x^{-\frac{1}{2}} \tilde{\mathbf{A}}_x \tilde{\mathbf{D}}_x^{-\frac{1}{2}} \mathbf{H}_x^{(l)} \mathbf{W}_x^{(l)}\right); \\ \mathbf{H}_s^{(l+1)} &= \text{ReLU}\left(\tilde{\mathbf{D}}_s^{-\frac{1}{2}} \tilde{\mathbf{A}}_s \tilde{\mathbf{D}}_s^{-\frac{1}{2}} \mathbf{H}_s^{(l)} \mathbf{W}_s^{(l)}\right), \end{aligned} \quad (5)$$

where $\mathbf{H}_x^{(l)}$ denotes the output embedding of the l -th GCN layer applied to the GEX graph. We define $\tilde{\mathbf{A}}_x = \mathbf{A}_x + \mathbf{I}$ as the expression-similarity adjacency matrix with self-loops, while $\tilde{\mathbf{D}}_x$ denotes its diagonal degree matrix, \mathbf{W}_x denotes the learnable weight matrix of the expression-graph convolution layer. Likewise, $\mathbf{H}_s^{(l)}$ represents the output embedding of the l -th GCN layer applied to the spatial graph. We define $\tilde{\mathbf{A}}_s = \mathbf{A}_s + \mathbf{I}$ as the spatial adjacency matrix with self-loops, denote its diagonal degree matrix by $\tilde{\mathbf{D}}_s$, while \mathbf{W}_s denotes the learnable weight matrix of the spatial-graph convolution layer.

3.2.2 Co-view Learning

Motivated by the inherent correlation between gene-expression patterns and tissue architecture, we model both modality-specific characteristics and their shared latent representations. To this end, we employ a GCN with shared parameters to learn joint embeddings for the two modalities. We formalize this with the following propagation rule:

$$\begin{aligned} \mathbf{H}_{s-co}^{(l+1)} &= \text{ReLU}\left(\tilde{\mathbf{D}}_s^{-\frac{1}{2}} \tilde{\mathbf{A}}_s \tilde{\mathbf{D}}_s^{-\frac{1}{2}} \mathbf{H}_{s-co}^{(l)} \mathbf{W}_{co}^{(l)}\right); \\ \mathbf{H}_{x-co}^{(l+1)} &= \text{ReLU}\left(\tilde{\mathbf{D}}_x^{-\frac{1}{2}} \tilde{\mathbf{A}}_x \tilde{\mathbf{D}}_x^{-\frac{1}{2}} \mathbf{H}_{x-co}^{(l)} \mathbf{W}_{co}^{(l)}\right), \end{aligned} \quad (6)$$

where $\mathbf{H}_{s-co}^{(l)}$ and $\mathbf{H}_{x-co}^{(l)}$ denote the output co-spatial and co-expression embeddings of the l -th co-convolution layer, respectively. \mathbf{W}_{co} denotes the shared learnable weight matrix of the co-convolution layer. With these two co-convolution embeddings for spatial locations and GEX profiles, we compute the final co-embedding \mathbf{H}_{co} as follows:

$$\mathbf{H}_{co}^{(l)} = \frac{1}{2}(\mathbf{H}_{s-co}^{(l)} + \mathbf{H}_{x-co}^{(l)}). \quad (7)$$

To ensure that the co-embedding captures biological patterns shared across both modalities and that the latent representations progressively align during optimization, we introduce a consistency loss that minimizes the divergence between \mathbf{H}_{s-co} and \mathbf{H}_{x-co} , formalized as follows:

$$\mathcal{L}_{\text{con}} = \|\tilde{\mathbf{H}}_{s-co} \tilde{\mathbf{H}}_{s-co}^T - \tilde{\mathbf{H}}_{x-co} \tilde{\mathbf{H}}_{x-co}^T\|_2^2, \quad (8)$$

where $\tilde{\mathbf{H}}_{s-co}$ and $\tilde{\mathbf{H}}_{x-co}$ denote the matrices obtained by normalizing \mathbf{H}_{s-co} and \mathbf{H}_{x-co} , respectively.

3.2.3 EPI-informed Learning

: The above-constructed EPI is represented as an image and further processed using a two-dimensional convolutional layer. This layer extracts high-dimensional feature maps from the input EPI by applying a ReLU activation and a following max-pooling operation, thereby downsampling the features while preserving salient topological information. In brief, we propose the following extended persistence embedding (EPE) formulation:

$$\begin{aligned} \text{EPE}_{i,j}^{(s)} &= \text{ReLU} \left(\sum_{m=0}^{k-1} \sum_{n=0}^{k-1} W_{m,n}^{(s)} \text{EPI}_{i\ell+m, j\ell+n}^{(s)} + b^{(s)} \right); \\ \text{EPE}_{i,j}^{(x)} &= \text{ReLU} \left(\sum_{m=0}^{k-1} \sum_{n=0}^{k-1} W_{m,n}^{(x)} \text{EPI}_{i\ell+m, j\ell+n}^{(x)} + b^{(x)} \right), \end{aligned} \quad (9)$$

where $\text{EPI}^{(s)}$ and $\text{EPI}^{(x)}$ denote the EPI for spatial locations and GEX profiles, respectively. $\mathbf{W}^{(s)}$, $\mathbf{W}^{(x)}$, $\mathbf{b}^{(s)}$, and $\mathbf{b}^{(x)}$ denote the learnable weight matrices and bias vectors. While k denotes the convolution kernel size, and ℓ denotes the stride length.

3.2.4 Multi-view Fusion

: To allocate the contributions of different modalities, we construct an attention-fusion layer that adaptively generates attention scores for each modality. Specifically, the attention score for each modality's EPE is computed as follows:

$$\begin{aligned} \mathbf{a}_{E_s} &= \text{softmax} \left(\mathbf{W}_2 \sigma(\mathbf{W}_1 \text{EPE}^{(s)} + \mathbf{b}_1) \right); \\ \mathbf{a}_{E_x} &= \text{softmax} \left(\mathbf{W}_2 \sigma(\mathbf{W}_1 \text{EPE}^{(x)} + \mathbf{b}_1) \right), \end{aligned} \quad (10)$$

where \mathbf{W}_1 and \mathbf{W}_2 denote learnable feature transformation matrices, respectively, and \mathbf{b}_1 is the bias vector. Accordingly, we assign attention weights a_s to the spatial embedding, a_x to the expression embedding, and a_{co} to the spatial-expression co-embedding. We then aggregate the above embeddings using the computed attention weights to produce the final representations as follows:

$$\begin{aligned} \mathbf{H} &= \text{MLP} \left(\mathbf{a}_{E_s} \cdot \text{EPE}^{(s)} + \mathbf{a}_{E_x} \cdot \text{EPE}^{(x)} \right. \\ &\quad \left. + a_s \mathbf{H}_s + a_x \mathbf{H}_x + a_{co} \mathbf{H}_{co} \right). \end{aligned} \quad (11)$$

3.3 Spatial Constraint and Distribution Optimization

Spatial transcriptomics data naturally contain spatial location information and exhibit a sparse, zero-inflated distribution. To leverage these two critical properties, we developed two design-optimization modules.

3.3.1 Spatial Constraint Optimization

To enhance the model's ability to learn from spatial locations, we propose a spatial-constraint module that explicitly preserves local neighborhood relationships in the embedding space. In brief, it operates via a two-part mechanism: (i) it increases the similarity between the embedding of cell i and those of its spatial neighbors ($j \in \mathcal{N}_i$), and (ii) it decreases the similarity with non-neighboring cells ($k \notin \mathcal{N}_i$) for both the co-embedding and the view-specific embeddings. This strategy is formalized as follows:

$$\begin{aligned} \mathcal{L}_{\text{sco}} &= - \sum_{i=1}^N \left[\sum_{j \in \mathcal{N}_i} \log \sigma(C(\mathbf{H}_i, \mathbf{H}_j)) + \sum_{j \in \mathcal{N}_i} \log \sum_{v=1}^V \exp(C(\mathbf{H}_i, \mathbf{H}_i^v)) \right. \\ &\quad \left. + \sum_{k \notin \mathcal{N}_i} \log(1 - \sigma(C(\mathbf{H}_i, \mathbf{H}_k))) + \sum_{k \notin \mathcal{N}_i} \log \sum_{v=1}^V \exp((1 - C(\mathbf{H}_i, \mathbf{H}_k)) C(\mathbf{H}_i, \mathbf{H}_k^v)) \right], \end{aligned} \quad (12)$$

where $C(\cdot)$ denotes the cosine similarity between two vectors, while σ denotes the hyperbolic tanh activation function. N denotes the number of cells in the spatial slice, and V denotes the number of views.

3.3.2 ZINB Distribution Optimization

Spatial transcriptomics data exhibit characteristic statistical properties: discrete counts with overdispersion and high sparsity. These properties can be modeled by a zero-inflated negative binomial (ZINB) distribution, whose mathematical form is given below:

$$\text{NB}(X = x | \mu, \theta) = \frac{\Gamma(x + \theta)}{x! \Gamma(\theta)} \left(\frac{\theta}{\theta + \mu} \right)^\theta \left(\frac{\mu}{\theta + \mu} \right)^x; \quad (13)$$

$$\text{ZINB}(X = x | \pi, \mu, \theta) = \pi I(x) + (1 - \pi) \text{NB}(x); \quad (14)$$

where μ and θ denote the mean and dispersion of gene expression, while π denotes the probability of zero inflation, $I(\cdot)$ denote the indicator function. To incorporate these characteristics into spatial domain identification, we employ a three-layer MLP $f(\cdot)$ to estimate the zero-inflation probability matrix $\mathbf{\Pi}$, the mean matrix \mathbf{M} , and the dispersion matrix $\mathbf{\Theta}$, as follows:

$$\begin{aligned} \mathbf{\Pi} &= \text{sigmoid}(\mathbf{W}_\pi f(\mathbf{H})); \\ \mathbf{M} &= \exp(\mathbf{W}_\mu f(\mathbf{H})); \\ \mathbf{\Theta} &= \exp(\mathbf{W}_\theta f(\mathbf{H})), \end{aligned} \quad (15)$$

where \mathbf{W}_π , \mathbf{W}_μ , and \mathbf{W}_θ denote the learnable weight matrices for $\mathbf{\Pi}$, \mathbf{M} , and $\mathbf{\Theta}$, respectively. To learn the model parameters, we minimize the negative log-likelihood of the ZINB model with respect to the observed X , which can be defined as follows:

$$\mathcal{L}_{\text{rec}} = - \sum \log(\text{ZINB}(X | \pi, \mu, \theta)). \quad (16)$$

3.4 The Total Loss Function

Ultimately, the fused embedding is jointly optimized using the consistency loss, the ZINB loss, and the spatial-constraint loss. We minimize the following total loss:

$$\mathcal{L}_f = \mathcal{L}_{\text{rec}} + \lambda_1 \mathcal{L}_{\text{con}} + \lambda_2 \mathcal{L}_{\text{sco}}, \quad (17)$$

where λ_1 and λ_2 denote the trade-off hyperparameters for respective loss function terms.

4 Experiments

4.1 Experiment Settings

4.1.1 Benchmark Datasets and Evaluation

The proposed SPHENIC model was evaluated on three publicly available spatial transcriptomics datasets, DLPFC (comprising 12 distinct tissue sections), 10x Visium human breast cancer dataset (HBC), and mouse brain anterior dataset (MBA) Maynard et al. (2021); Buache et al. (2011). Clustering performance was assessed using the adjusted Rand index (ARI) and normalized mutual information (NMI).

4.1.2 Compared Methods

To enable a fair comparison, we benchmark our model against eight representative methods: SCANPY Wolf et al. (2018), SpaGCN Hu et al. (2021), stLearn Pham et al. (2020), SCGDL Liu et al. (2023), DeepST Xu et al. (2022), GraphST Long et al. (2023), stMMR Zhang et al. (2024), and Spatial-MGCN Wang et al. (2023).

4.1.3 Implementation Details

All experiments were conducted on a single NVIDIA virtual GPU (vGPU) rented from AutoDL, providing up to 48 GB of memory, and a 25-core Intel Xeon Platinum 8481C processor. The model was implemented in PyTorch 2.1.0 and executed with CUDA 12.1. For each dataset, training was terminated after 100 epochs. All baseline methods were run with the default hyper-parameters recommended in their original publications.

Metric	Dataset	Methods								
		SCANPY	SpaGCN	stLearn	SCGDL	DeepST	GraphST	stMMR	Spatial-MGCN	SPHENIC
ARI	HBC	0.4852 _{0.0014}	0.5679 _{0.0281}	0.5502 _{0.0336}	0.3288 _{0.0251}	0.5630 _{0.0089}	0.5183 _{0.0057}	0.6492 _{0.0105}	0.6404 _{0.0324}	0.6823 _{0.0236}
	MBA	0.3965 _{0.0095}	0.3442 _{0.0089}	0.3413 _{0.0019}	0.2581 _{0.0123}	0.2591 _{0.0343}	0.2933 _{0.0013}	0.4225 _{0.0218}	0.3958 _{0.0002}	0.4879 _{0.0168}
	151507	0.2553 _{0.0123}	0.3826 _{0.0305}	0.4295 _{0.0104}	0.4626 _{0.0241}	0.5224 _{0.0276}	0.4479 _{0.0030}	0.5858 _{0.0006}	0.6268 _{0.0460}	0.6533 _{0.0174}
	151508	0.1425 _{0.0070}	0.3948 _{0.0215}	0.4003 _{0.0068}	0.3554 _{0.0182}	0.4289 _{0.0577}	0.3518 _{0.0101}	0.5184 _{0.0043}	0.5066 _{0.0104}	0.5354 _{0.0489}
	151509	0.1431 _{0.0117}	0.3408 _{0.0239}	0.2952 _{0.0075}	0.3737 _{0.0340}	0.4760 _{0.0647}	0.3671 _{0.0581}	0.5873 _{0.0238}	0.5810 _{0.0387}	0.6051 _{0.0614}
	151510	0.1704 _{0.0052}	0.3836 _{0.0326}	0.3409 _{0.0433}	0.3057 _{0.0034}	0.4657 _{0.0211}	0.3973 _{0.0405}	0.7071 _{0.0045}	0.5706 _{0.0364}	0.5397 _{0.0341}
	151669	0.2550 _{0.0286}	0.2670 _{0.0479}	0.2523 _{0.0019}	0.2515 _{0.0084}	0.2773 _{0.0181}	0.2998 _{0.0575}	0.4569 _{0.0115}	0.4514 _{0.0591}	0.4904 _{0.0535}
	151670	0.2434 _{0.0161}	0.2380 _{0.0288}	0.2346 _{0.0060}	0.2094 _{0.0159}	0.2856 _{0.0276}	0.2597 _{0.0145}	0.4017 _{0.0200}	0.4267 _{0.0579}	0.4260 _{0.0561}
	151671	0.2197 _{0.0158}	0.4076 _{0.0108}	0.3322 _{0.0478}	0.2343 _{0.0026}	0.3724 _{0.0375}	0.3883 _{0.0095}	0.5178 _{0.0257}	0.6575 _{0.0061}	0.6514 _{0.0640}
	151672	0.2168 _{0.0311}	0.4781 _{0.0574}	0.4039 _{0.0614}	0.3154 _{0.0276}	0.4320 _{0.0514}	0.4213 _{0.0087}	0.5915 _{0.0054}	0.7534 _{0.0389}	0.7365 _{0.0213}
	151673	0.1746 _{0.0190}	0.4473 _{0.0104}	0.3534 _{0.0269}	0.3248 _{0.0103}	0.5282 _{0.0054}	0.4800 _{0.0228}	0.6154 _{0.0047}	0.5692 _{0.0493}	0.5817 _{0.0214}
	151674	0.2395 _{0.0197}	0.3326 _{0.0297}	0.3060 _{0.0276}	0.2341 _{0.0078}	0.5451 _{0.0319}	0.4403 _{0.0365}	0.5063 _{0.0040}	0.5610 _{0.0171}	0.5641 _{0.0286}
	151675	0.2259 _{0.0299}	0.3340 _{0.0475}	0.3922 _{0.0323}	0.2341 _{0.0065}	0.5513 _{0.0303}	0.4518 _{0.0282}	0.5420 _{0.0022}	0.5543 _{0.0156}	0.5203 _{0.0322}
	151676	0.1678 _{0.0114}	0.3214 _{0.0171}	0.3512 _{0.0052}	0.2554 _{0.0463}	0.5071 _{0.0248}	0.3816 _{0.0105}	0.5826 _{0.0024}	0.5666 _{0.0072}	0.5233 _{0.0124}
NMI	HBC	0.6060 _{0.0021}	0.6571 _{0.0059}	0.6647 _{0.0184}	0.4828 _{0.0568}	0.6933 _{0.0058}	0.6586 _{0.0039}	0.6916 _{0.0041}	0.6941 _{0.0188}	0.6954 _{0.0188}
	MBA	0.6389 _{0.0019}	0.6488 _{0.0151}	0.6455 _{0.0004}	0.6204 _{0.0036}	0.5523 _{0.0275}	0.6769 _{0.0015}	0.6732 _{0.0014}	0.6365 _{0.0199}	0.6909 _{0.0165}
	151507	0.3436 _{0.0067}	0.4961 _{0.0340}	0.5435 _{0.0055}	0.5296 _{0.0126}	0.6454 _{0.0399}	0.5740 _{0.0069}	0.7179 _{0.0026}	0.7092 _{0.0103}	0.7408 _{0.0213}
	151508	0.1954 _{0.0103}	0.5104 _{0.0135}	0.5157 _{0.0076}	0.4561 _{0.0016}	0.5681 _{0.0456}	0.5257 _{0.0060}	0.6414 _{0.0089}	0.6042 _{0.0238}	0.6312 _{0.0116}
	151509	0.2600 _{0.0051}	0.5135 _{0.0352}	0.4901 _{0.0096}	0.5134 _{0.0118}	0.6292 _{0.0187}	0.5374 _{0.0158}	0.7148 _{0.0097}	0.6708 _{0.0228}	0.6961 _{0.0027}
	151510	0.2629 _{0.0193}	0.4988 _{0.0384}	0.4777 _{0.0203}	0.4734 _{0.0042}	0.6126 _{0.0108}	0.5470 _{0.0070}	0.7189 _{0.0026}	0.6539 _{0.0272}	0.6563 _{0.0088}
	151669	0.2679 _{0.0108}	0.4541 _{0.0629}	0.4518 _{0.0067}	0.4126 _{0.0061}	0.5216 _{0.0093}	0.5102 _{0.0271}	0.5641 _{0.0434}	0.5948 _{0.0634}	0.6184 _{0.0048}
	151670	0.2473 _{0.0405}	0.4224 _{0.0190}	0.4379 _{0.0122}	0.3675 _{0.0130}	0.5165 _{0.0208}	0.4576 _{0.0164}	0.5417 _{0.0423}	0.5513 _{0.0260}	0.6023 _{0.0152}
	151671	0.2334 _{0.0253}	0.5550 _{0.0148}	0.5076 _{0.0153}	0.4004 _{0.0045}	0.5884 _{0.0332}	0.5727 _{0.0077}	0.6676 _{0.0140}	0.6341 _{0.0042}	0.7350 _{0.0219}
	151672	0.1757 _{0.0158}	0.5956 _{0.0333}	0.5207 _{0.0134}	0.4538 _{0.0406}	0.6005 _{0.0370}	0.5779 _{0.0053}	0.6837 _{0.0026}	0.7453 _{0.0252}	0.7133 _{0.0153}
	151673	0.2944 _{0.0173}	0.5908 _{0.0120}	0.5192 _{0.0076}	0.4304 _{0.0046}	0.6771 _{0.0066}	0.6254 _{0.0146}	0.6808 _{0.0151}	0.6708 _{0.0214}	0.6863 _{0.0094}
	151674	0.3066 _{0.0139}	0.4586 _{0.0148}	0.4952 _{0.0222}	0.3633 _{0.0093}	0.6431 _{0.0288}	0.5532 _{0.0248}	0.6074 _{0.0025}	0.6494 _{0.0193}	0.6556 _{0.0121}
	151675	0.3124 _{0.0347}	0.4715 _{0.0637}	0.4877 _{0.0147}	0.3980 _{0.0076}	0.6648 _{0.0291}	0.5758 _{0.0107}	0.6431 _{0.0168}	0.6757 _{0.0045}	0.6360 _{0.0162}
	151676	0.2787 _{0.0081}	0.4773 _{0.0120}	0.4720 _{0.0094}	0.4061 _{0.0226}	0.6682 _{0.0155}	0.5320 _{0.0072}	0.6868 _{0.0017}	0.6699 _{0.0075}	0.6423 _{0.0188}

Table 1: Experimental results of nine methods on the fourteen distinct spatial transcriptomic slices.

4.2 Clustering Performance

The comparative performance of nine methods is summarized in Table 1. Fig. 3 provides a visual comparison of the clustering outputs produced by each method. These results reveal that:

(i) SPHENIC delivers state-of-the-art clustering accuracy in architecturally complex tissues. With respect to ARI, SPHENIC exceeds the next-best method (stMMR) by 3.31% on the HBC dataset and 6.54% on the mouse-anterior dataset, underscoring its strength in identifying domains within challenging tissue architectures.

(ii) In spatially simpler structures such as the DLPCF slices, SPHENIC surpasses the next-best method (Spatial-MGCN for slice 151507 and stMMR for slices 151508 and 151569) by 2.65%, 1.70%, and 3.35% ARI, respectively. These findings confirm SPHENIC’s generalizability and its ability to extract fundamental biological signals irrespective of spatial complexity.

(iii) SPHENIC accurately delineates tumor boundaries in the HBC dataset, as illustrated in Fig. 3. SPHENIC shows strong agreement with manual annotations in identifying key tumor-microenvironment components (e.g., ‘IDC_4’, ‘healthy_1’). Unlike baselines that yield fragmented clusters and tumor-immune misclassifications, SPHENIC preserves biologically valid structures, achieving expert-level spatial recognition in carcinomas.

4.3 Ablation Study

To demonstrate the effectiveness of the proposed modules, we construct several variants of SPHENIC: ‘w/o Topo’, which omits the invariant topological feature-extraction module; ‘w/o SCDOM’, which excludes the spatial-constraint and distribution-optimization module; and ‘w/o Both’, which removes both modules. As shown in Table 2, omitting the topological module (‘w/o Topo’) reduces ARI by 4.84 % and 3.30 % relative to the full model, thereby validating the contribution of the topological learning component. Similarly, removing the spatial-constraint and distribution-optimization module (‘w/o SCDOM’) decreases ARI by 5.57 % and 2.80 %, confirming the importance of explicitly modeling spatial neighbourhoods and non-neighbourhoods. We further evaluate a variant lacking both modules. The complete SPHENIC model improves ARI by 6.00 % and 4.39 % over this ablated variant, demonstrating the synergistic benefit of combining topological and spatial-constraint learning.

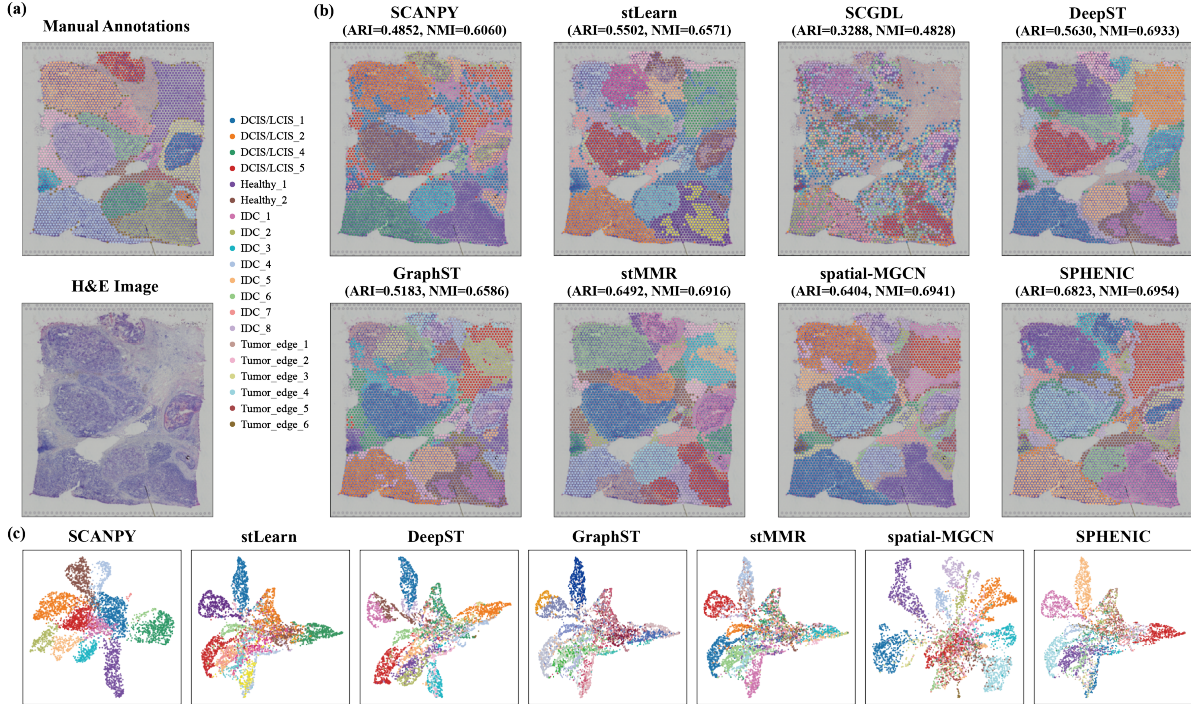


Figure 3: Comparison experiments on HBC dataset between SPHENIC and other baselines. (a) Manual ground-truth annotations and histological image of the HBC dataset. (b) Spatial clustering result visualization by SCANPY, stLearn, SCGDL, DeepST, GraphST, stMMR, spatial-MGCN, and SPHENIC. (c) UMAP visualization of detected clusters by the above baselines.

Methods	HBC		151507	
	ARI	NMI	ARI	NMI
w/o Topo	0.6339 _{0.0423}	0.6494 _{0.0271}	0.6203 _{0.0265}	0.7178 _{0.0170}
w/o SCDOM	0.6266 _{0.0520}	0.6369 _{0.0442}	0.6253 _{0.0320}	0.6780 _{0.0337}
w/o Both	0.6223 _{0.0446}	0.6286 _{0.0361}	0.6094 _{0.0174}	0.6562 _{0.0190}
SPHENIC	0.6823 _{0.0236}	0.6954 _{0.0188}	0.6533 _{0.0174}	0.7408 _{0.0213}

Table 2: Ablation results of SPHENIC on three datasets. 'w/o' means 'SPHENIC without'.

4.4 Model Analysis

4.4.1 Hyperparameter Sensitivity Analysis

We evaluate the effect of hyperparameters on the performance of SPHENIC in the HBC dataset and DLPFC-151507 dataset, which includes the trade-off coefficients of the loss function (λ_1 and λ_2). Fig. 4 demonstrates the ARI of SPHENIC when λ_1 and λ_2 are varied from 10^{-3} to 10^3 . From this figure, the proposed SPHENIC is insensitive to both λ_1 and λ_2 in the range 10^{-3} to 10^{-1} , further illustrates the robustness of our proposed SPHENIC.

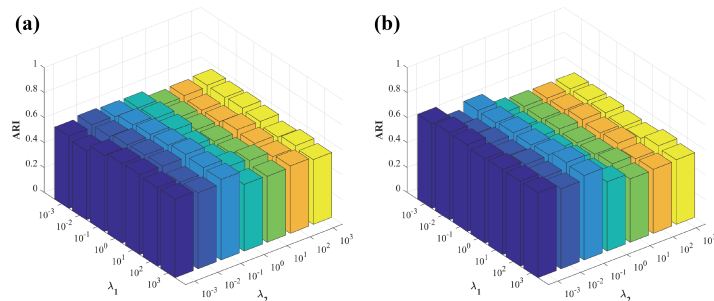


Figure 4: The hyperparameter analysis on HBC dataset, DLPFC-151507, respectively, in ARI term.

4.4.2 Visualization Analysis

In addition, to further verify the effectiveness of SPHENIC, we visualize the spatial clustering results of SPHENIC in different training stages (0%, 33%, 67% and 100% training epochs) by the UMAP methods in Fig. 5 McInnes et al. (2018). We can clearly observed that the spatial clustering structure of our multi-view fused embedding H progressively refines across training epochs, along with consistent improvement in both ARI and NMI term.

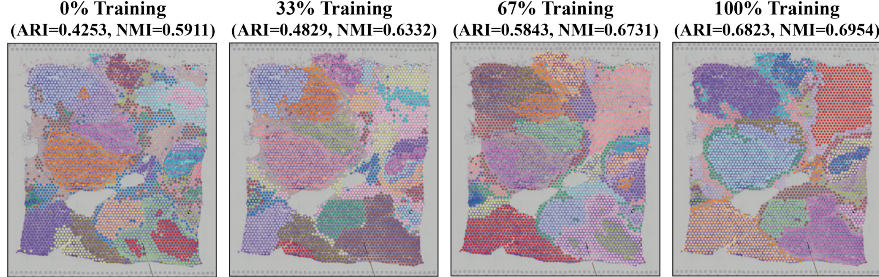


Figure 5: The visualization results of spatial clustering by SPHENIC model in different training stages

4.4.3 Gene Imputation Analysis

To validate SPHENIC’s dual-module strategy in preserving spatial expression patterns while reducing noise artifacts, we evaluated its performance on the HBC dataset by examining the spatial distributions of characteristic marker genes (*DSP*, *IFT122*, *CCL21*, *CTTN*, *GNG5*, *FARP1*). Figure 6 in the appendix shows that SPHENIC successfully reconstructs biologically plausible expression patterns while significantly reducing technical noise compared to raw data. The system maintains consistent spatial distributions of these markers that align with established biological knowledge, confirming its ability to (i) filter out non-informative noise, (ii) recover true biological signals from degraded data, and (iii) faithfully reconstruct spatial expression profiles.

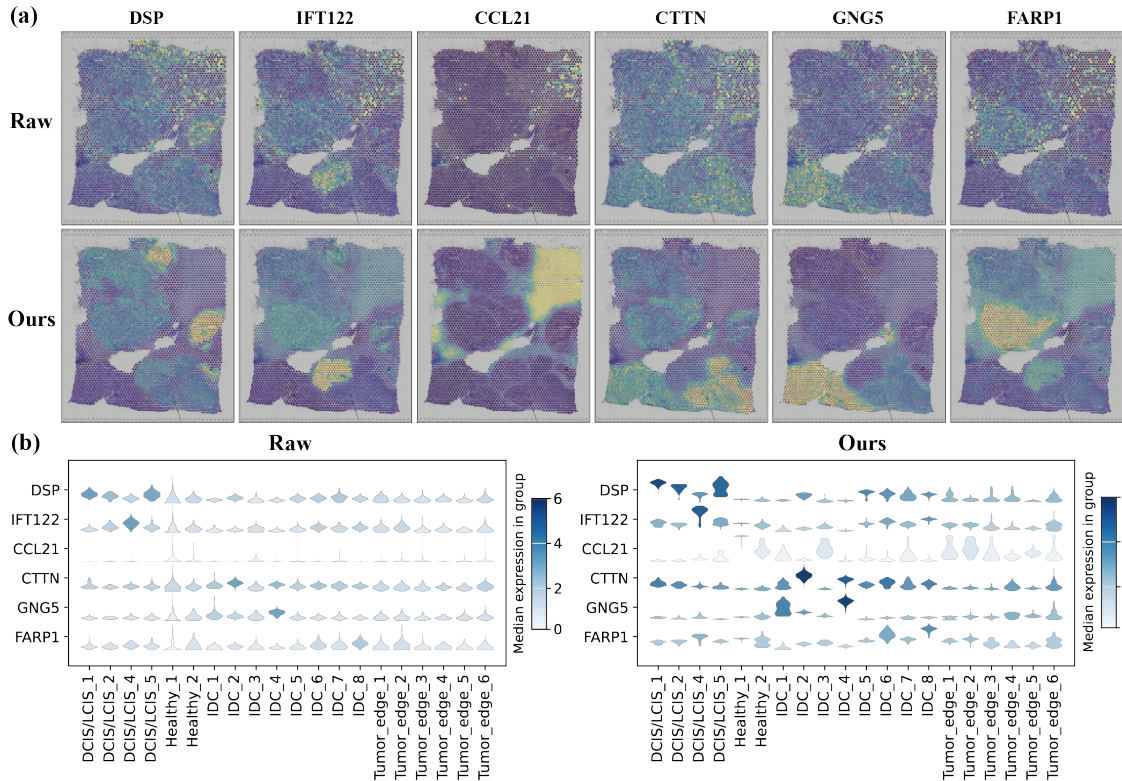


Figure 6: Gene imputation results in HBC dataset. (a) The visualization of raw expression of cluster marker genes and expression after SPHENIC imputation. (b) The violin plots of raw marker gene expression and SPHENIC imputed gene expression.

5 Conclusion

In this paper, we present SPHENIC, a topology-informed clustering framework for spatial transcriptomics data. By leveraging persistent feature, the model learns more robust topological information and is less sensitive to noise. Meanwhile, we leverage spatial coordinates to supervise the embedding space, forcing proximity between a cell's embedding and those of its spatial neighbors while separating it from non-neighboring cells, thereby producing high-quality spatial embeddings. Extensive validation experiments demonstrate the superiority of the proposed SPHENIC. Nevertheless, the principal limitation of our approach is the computational overhead associated with extended persistent homology, which may impede scalability in application scenarios.

References

- Blondel, V. D., Guillaume, J.-L., Lambiotte, R., and Lefebvre, E. (2008). Fast unfolding of communities in large networks. *Journal of statistical mechanics: theory and experiment*, 2008(10):P10008.
- Buache, E., Etique, N., Alpy, F., Stoll, I., Muckensturm, M., Reina-San-Martin, B., Chenard, M., Tomasetto, C., and Rio, M. (2011). Deficiency in trefoil factor 1 (tff1) increases tumorigenicity of human breast cancer cells and mammary tumor development in tff1-knockout mice. *Oncogene*, 30(29):3261–3273.
- Chen, C., Ni, X., Bai, Q., and Wang, Y. (2019). A topological regularizer for classifiers via persistent homology. In Chaudhuri, K. and Sugiyama, M., editors, *Proceedings of the Twenty-Second International Conference on Artificial Intelligence and Statistics*, volume 89 of *Proceedings of Machine Learning Research*, pages 2573–2582. PMLR.
- Chen, Y., Frias, J., and Gel, Y. R. (2024). Topogcl: Topological graph contrastive learning. In *Proceedings of the AAAI conference on artificial intelligence*, volume 38, pages 11453–11461.
- Gulati, G. S., D'Silva, J. P., Liu, Y., Wang, L., and Newman, A. M. (2025). Profiling cell identity and tissue architecture with single-cell and spatial transcriptomics. *Nature Reviews Molecular Cell Biology*, 26(1):11–31.
- Guo, C.-K., Xia, C.-R., Peng, G., Cao, Z.-J., and Gao, G. (2025). Learning phenotype associated signature in spatial transcriptomics with passage. *Small Methods*, 9(5):2401451.
- Hernández-Lemus, E., Miramontes, P., and Martínez-García, M. (2024). Topological data analysis in cardiovascular signals: An overview. *Entropy*, 26(1):67.
- Hu, J., Li, X., Coleman, K., Schroeder, A., Ma, N., Irwin, D. J., Lee, E. B., Shinohara, R. T., and Li, M. (2021). Spagcn: Integrating gene expression, spatial location and histology to identify spatial domains and spatially variable genes by graph convolutional network. *Nature methods*, 18(11):1342–1351.
- Hu, Y., Xie, M., Li, Y., Rao, M., Shen, W., Luo, C., Qin, H., Baek, J., and Zhou, X. M. (2024). Benchmarking clustering, alignment, and integration methods for spatial transcriptomics. *Genome Biology*, 25(1):212.
- Jain, S. and Eadon, M. T. (2024). Spatial transcriptomics in health and disease. *Nature Reviews Nephrology*, 20(10):659–671.
- Kipf, T. (2016). Semi-supervised classification with graph convolutional networks. *arXiv preprint arXiv:1609.02907*.
- Li, S., Hua, H., and Chen, S. (2025). Graph neural networks for single-cell omics data: a review of approaches and applications. *Briefings in Bioinformatics*, 26(2).
- Liu, T., Fang, Z.-Y., Li, X., Zhang, L.-N., Cao, D.-S., and Yin, M.-Z. (2023). Graph deep learning enabled spatial domains identification for spatial transcriptomics. *Briefings in Bioinformatics*, 24(3):bbad146.
- Liu, T., Fang, Z.-Y., Zhang, Z., Yu, Y., Li, M., and Yin, M.-Z. (2024). A comprehensive overview of graph neural network-based approaches to clustering for spatial transcriptomics. *Computational and Structural Biotechnology Journal*, 23:106–128.
- Long, Y., Ang, K. S., Li, M., Chong, K. L. K., Sethi, R., Zhong, C., Xu, H., Ong, Z., Sachaphibulkij, K., Chen, A., et al. (2023). Spatially informed clustering, integration, and deconvolution of spatial transcriptomics with graphst. *Nature Communications*, 14(1):1155.
- Maynard, K. R., Collado-Torres, L., Weber, L. M., Uyttingco, C., Barry, B. K., Williams, S. R., Catallini, J. L., Tran, M. N., Besich, Z., Tippani, M., et al. (2021). Transcriptome-scale spatial gene expression in the human dorsolateral prefrontal cortex. *Nature neuroscience*, 24(3):425–436.
- McInnes, L., Healy, J., and Melville, J. (2018). Umap: Uniform manifold approximation and projection for dimension reduction. *arXiv preprint arXiv:1802.03426*.
- Moses, L. and Pachter, L. (2022). Museum of spatial transcriptomics. *Nature methods*, 19(5):534–546.

- Pham, D., Tan, X., Xu, J., Grice, L. F., Lam, P. Y., Raghobar, A., Vukovic, J., Ruitenber, M. J., and Nguyen, Q. (2020). stlearn: integrating spatial location, tissue morphology and gene expression to find cell types, cell-cell interactions and spatial trajectories within undissociated tissues. *bioRxiv*, pages 2020–05.
- Pham, P., Bui, Q.-T., Nguyen, N. T., Kozma, R., Yu, P. S., and Vo, B. (2025). Topological data analysis in graph neural networks: Surveys and perspectives. *IEEE Transactions on Neural Networks and Learning Systems*.
- Rao, A., Barkley, D., França, G. S., and Yanai, I. (2021). Exploring tissue architecture using spatial transcriptomics. *Nature*, 596(7871):211–220.
- Satija, R., Farrell, J. A., Gennert, D., Schier, A. F., and Regev, A. (2015). Spatial reconstruction of single-cell gene expression data. *Nature biotechnology*, 33(5):495–502.
- Skaf, Y. and Laubenbacher, R. (2022). Topological data analysis in biomedicine: A review. *Journal of Biomedical Informatics*, 130:104082.
- Su, Z., Liu, X., Hamdan, L. B., Maroulas, V., Wu, J., Carlsson, G., and Wei, G.-W. (2025). Topological data analysis and topological deep learning beyond persistent homology—a review. *arXiv preprint arXiv:2507.19504*.
- Tian, L., Chen, F., and Macosko, E. Z. (2023). The expanding vistas of spatial transcriptomics. *Nature Biotechnology*, 41(6):773–782.
- Traag, V. A., Waltman, L., and Van Eck, N. J. (2019). From louvain to leiden: guaranteeing well-connected communities. *Scientific reports*, 9(1):1–12.
- Wang, B., Luo, J., Liu, Y., Shi, W., Xiong, Z., Shen, C., and Long, Y. (2023). Spatial-mgcn: a novel multi-view graph convolutional network for identifying spatial domains with attention mechanism. *Briefings in Bioinformatics*, 24(5):bbad262.
- Wang, Z., Geng, A., Duan, H., Cui, F., Zou, Q., and Zhang, Z. (2024). A comprehensive review of approaches for spatial domain recognition of spatial transcriptomes. *Briefings in Functional Genomics*, 23(6):702–712.
- Wasserman, L. (2018). Topological data analysis. *Annual review of statistics and its application*, 5(2018):501–532.
- Williams, C. G., Lee, H. J., Asatsuma, T., Vento-Tormo, R., and Haque, A. (2022). An introduction to spatial transcriptomics for biomedical research. *Genome medicine*, 14(1):68.
- Wolf, F. A., Angerer, P., and Theis, F. J. (2018). Scanpy: large-scale single-cell gene expression data analysis. *Genome biology*, 19(1):15.
- Xu, C., Jin, X., Wei, S., Wang, P., Luo, M., Xu, Z., Yang, W., Cai, Y., Xiao, L., Lin, X., et al. (2022). Deepst: identifying spatial domains in spatial transcriptomics by deep learning. *Nucleic Acids Research*, 50(22):e131–e131.
- Yan, W., Zhang, Y., Lv, C., Tang, C., Yue, G., Liao, L., and Lin, W. (2023). Gcfagg: Global and cross-view feature aggregation for multi-view clustering. In *Proceedings of the IEEE/CVF Conference on Computer Vision and Pattern Recognition (CVPR)*, pages 19863–19872.
- Yuan, Z., Zhao, F., Lin, S., Zhao, Y., Yao, J., Cui, Y., Zhang, X.-Y., and Zhao, Y. (2024). Benchmarking spatial clustering methods with spatially resolved transcriptomics data. *Nature Methods*, 21(4):712–722.
- Zahedi, R., Ghamsari, R., Argha, A., Macphillamy, C., Beheshti, A., Alizadehsani, R., Lovell, N. H., Lotfollahi, M., and Alinejad-Rokny, H. (2024). Deep learning in spatially resolved transcriptomics: a comprehensive technical view. *Briefings in Bioinformatics*, 25(2):bbae082.
- Zhang, D., Yu, N., Yuan, Z., Li, W., Sun, X., Zou, Q., Li, X., Liu, Z., Zhang, W., and Gao, R. (2024). stmmr: accurate and robust spatial domain identification from spatially resolved transcriptomics with multimodal feature representation. *GigaScience*, 13:giae089.
- Zhang, Y., Liu, Y., Ma, Z., Li, M., Xu, C., and Gong, H. (2025). Improving diffusion-based protein backbone generation with global-geometry-aware latent encoding. *Nature Machine Intelligence*, pages 1–15.